Ab initio time-dependent density-functional-theory study of the frequency comb structure, coherence, and dephasing of multielectron systems in the vuv-xuv regimes via high-order harmonic generation

Juan J. Carrera[1] and Shih-I Chu[1,2,*]

[1]*Department of Physics, Center for Quantum Science and Engineering, National Taiwan University, Taipei 10617, Taiwan*

[2]*Department of Chemistry, University of Kansas, Lawrence, Kansas 66045, USA*

(Received 30 April 2008; revised manuscript received 17 March 2009; published 17 June 2009)

We present an *ab initio* nonperturbative investigation of the frequency comb structure and coherence within each order of the high-order harmonic generation (HHG) of rare-gas atoms by means of the time-dependent density-functional theory (TDDFT) with optimized effective potential (OEP) and self-interaction correction (SIC). The TDDFT+OEP-SIC equations are solved accurately and efficiently by means of the time-dependent generalized pseudospectral technique. We found that a nested comb structure appears within each order of the harmonics, ranging from the first harmonic all the way to the cutoff region. We explore in detail the temporal coherence and robustness of the comb structure by varying the laser-pulse separation τ, the number of pulses N, the phase difference between pulses $\Delta\phi$, and the laser intensity. The frequency comb structure and coherence are preserved in each harmonic regardless of the values of τ and N used for the case of weak and medium strong incident laser-pulse trains. The time-frequency characteristics of the HHG coherence structure are analyzed in details by means of the wavelet transform of the time-dependent induced dipoles. The interference modulation can be attributed to the constant phase relationship of harmonics among successive pulses. However, under superstrong fields, nonuniform and substantial ionization takes place during each pulse, jeopardizing the temporal coherence of the emitted frequency comb modes. Finally, we found that the dynamical electron correlation, which is included in the present TDDFT+OEP-SIC treatment but not in the single-active-electron model, is significant for the quantitative exploration of the frequency comb structure and coherence of higher harmonics.

DOI: 10.1103/PhysRevA.79.063410 PACS number(s): 32.80.Rm, 42.65.Ky, 31.15.A−, 42.62.Eh

I. INTRODUCTION

Recently, advancements in femtosecond laser-based optical frequency combs have led to dramatic impact to ultrahigh precision optical frequency metrology [1–4], atomic clocks [5,6], and ultrafast laser science [7,8]. For a train of identical pulses, separated by a fixed time interval τ, its Fourier transform yields a spectrum consisting of a comb of regularly spaced frequencies [9]. The optical frequencies f_n of the comb lines can be written as $f_n=nf_r+f_0$, where n is a large integer, $f_r=1/\tau$ is the repetition frequency, and f_0 is the carrier-envelope offset frequency. The frequency comb produces a "ruler" in the frequency domain with which an unknown optical frequency can be measured. For precision spectroscopy, a frequency comb laser provides a phase-coherent link between the radio frequency of an atomic clock and the optical frequency of a stabilized narrow-band continuous-wave (cw) laser used for the actual spectroscopy. However, suitable narrow-band-width cw sources rarely exist at high frequencies [10], such as vacuum-ultraviolet (vuv) and extreme-ultraviolet (xuv) radiations.

More recently, coherent vuv [11] and xuv [12] radiations at a repetition frequency of more than 100 MHz, a 1000-fold improvement over previous experiment [13], have been explored experimentally via high-order harmonic generation (HHG). If the high-frequency comb laser can be generated successfully, there will be a number of applications such as vuv-xuv holography, nanolithography, x-ray atomic clocks, and for the testing of fundamental theories such as quantum electrodynamics. However, there are currently some experimental difficulties in the observation of the frequency comb structure within each harmonic order, with the exception of the third-order harmonic case [11]. Accurate theoretical exploration of the frequency comb structure and coherence within each high harmonic is thus of timely importance and will facilitate further experimental development of the frequency comb laser in the vuv-xuv regimes. In a recent paper, we have initiated such a theoretical study for the atomic hydrogen system [14]. The time-dependent Schrödinger equation is solved accurately by means of the time-dependent generalized pseudospectral (TDGPS) method [15]. We found that a nested comb structure appears within each of the harmonics, ranging from the first harmonic all the way to the cutoff harmonics. This suggests that the experimental observation of the frequency comb structure in the vuv-xuv regimes will become feasible when the spectral resolution is improved.

In this paper, we extend the *ab initio* study to the rare-gas atoms, particularly, the helium atoms, which are one of the most common systems used in the experimental studies of HHG and comb laser. One of the goals is to investigate the effect of electron correlation on the comb structure and coherence. The *self-interaction-free* time-dependent density-functional theory (TDDFT) recently developed [16,17] is extended for the *ab initio* treatment of the frequency comb structure and coherence within each order of high harmonics. In addition, we also present the single-active-electron (SAE) model calculation for comparison. Finally, we investigate the effect of ionization dephasing and intensity-dependent phase

*sichu@ku.edu

shifts on the frequency comb structure and coherence. The results presented in this article are of current interest and significance to the experimental realization of phase-coherent frequency combs in the vuv-xuv regimes [11,12].

The paper is organized as follows. In Sec. II, we briefly outline the self-interaction-free TDDFT procedure and associated TDGPS computational techniques for accurate nonperturbative treatment of HHG and frequency comb processes. Comparison of the all-electron TDDFT data to the SAE model results is also presented. In Sec. III, we present the wavelet time-frequency analysis of the comb spectrum. The effect of ionization dephasing on the frequency coherence in intense laser fields is explored in Sec. IV. This is followed by a conclusion in Sec. V.

II. SELF-INTERACTION-FREE TDDFT FOR THE TREATMENT OF FREQUENCY COMB STRUCTURE AND COHERENCE

To understand the mode structure of a frequency comb emitted by a mode-locked laser, consider the pulse circulating in a laser cavity [9]. Since the group velocity of the pulse envelope and the phase velocity of the carrier wave are not equal, there is a phase shift $\Delta\phi$ from pulse to pulse. The angular frequency spectrum emanating from such a pulse train gives rise to comb lines, spaced by the repetition angular frequency $\omega_r=2\pi/\tau$ and the offset carrier envelope frequency $\omega_0=\Delta\phi\omega_r/2\pi$. The comb angular frequencies $\omega_{m'}$ are given by

$$\omega_{m'} = m'\omega_r + \omega_0, \tag{1}$$

where m' is an integer index and typically on the order of 10^5-10^6 [12].

To pursue the exploration of the detailed comb structure of each high-order harmonic, we perform accurate calculations of the time-dependent wave function, induced dipole moments, and HHG power spectra of He atoms by means of the TDDFT with optimized effective potential (OEP) [16,18,19] and self-interaction correction (SIC) [16,17]. The central equation of the TDDFT+OEP-SIC formalism for the treatment of multiphoton processes of many-electron atomic systems in a sequence of intense laser pulses is given by, in atomic units,

$$i\frac{\partial}{\partial t}\psi_{i\sigma}(\mathbf{r},t) = \hat{H}(\mathbf{r},t)\psi_{i\sigma}(\mathbf{r},t) = [\hat{H}_0(\mathbf{r}) + \hat{V}(\mathbf{r},t)]\psi_{i\sigma}(\mathbf{r},t),$$
$$i = 1,2,\ldots,N_\sigma, \tag{2}$$

where $\hat{H}_0(\mathbf{r})=-\frac{1}{2}\nabla^2+V^{\mathrm{OEP}}_{\mathrm{SIC},\sigma}(\mathbf{r},0)$ is the field-free Hamiltonian with an OEP and SIC at $t=0$ and σ is the spin index. $\hat{V}(\mathbf{r},t)$ contains the electric-dipole coupling to the laser field and the residual time-dependent OEP with SIC [16,17],

$$\hat{V}(\mathbf{r},t) = -\mathbf{F}_0\cdot\mathbf{r}E(t) + V^{\mathrm{OEP}}_{\mathrm{SIC},\sigma}(\mathbf{r},t) - V^{\mathrm{OEP}}_{\mathrm{SIC},\sigma}(\mathbf{r},0), \tag{3}$$

where

$$E(t) = \sum_{n=1}^{N}\hat{E}(t-n\tau)\exp[i(\omega_c t - n\omega_c\tau + n\Delta\phi)], \tag{4}$$

where $\hat{E}(t)$ is the Gaussian envelope function, F_0 is the laser electric field amplitude, τ is the pulse separation, and N is the total number of excitation pulses. The frequency comb has a centered mode at ω_c and its frequency spectrum is related to Eq. (1) by absorbing integer multiples of ω_r contained in ω_c and renumbering the comb modes, namely,

$$\omega_{m'} = m'\omega_r + \omega_0 = n'\omega_r + \omega_c. \tag{5}$$

The time-dependent OEP-SIC potential, $V^{\mathrm{OEP}}_{\mathrm{SIC},\sigma}(\mathbf{r},t)$, is determined as follows [16,17]:

$$V^{\mathrm{OEP}}_{\mathrm{SIC},\sigma}(\mathbf{r},t) = v_{ext}(\mathbf{r},t) + \int\frac{\rho(\mathbf{r}',t)}{|\mathbf{r}-\mathbf{r}'|}d^3\mathbf{r}' + V^{\mathrm{SIC}}_{xc,\sigma}(\mathbf{r},t), \tag{6}$$

where $v_{ext}(\mathbf{r},t)$ is the external potential, $\rho(\mathbf{r},t)$ is the electron density, and the exchange-correlation (xc) potential with SIC is given by

$$V^{\mathrm{SIC}}_{\mathrm{xc},\sigma}(\mathbf{r},t) = \sum_i\frac{\rho_{i\sigma}(\mathbf{r},t)}{\rho_\sigma(\mathbf{r},t)}\{v_{i\sigma}(\mathbf{r},t) + [\bar{V}^{\mathrm{SIC}}_{\mathrm{xc},i\sigma}(t) - \bar{v}_{i\sigma}(t)]\}, \tag{7}$$

with

$$v_{i\sigma}(\mathbf{r},t) = -\int\frac{\rho_{i\sigma}(\mathbf{r}',t)}{|\mathbf{r}-\mathbf{r}'|}d^3\mathbf{r}' - \frac{\delta E_{\mathrm{xc}}[\rho_{i\sigma},0]}{\delta\rho_{i\sigma}(\mathbf{r},t)}, \tag{8}$$

and $\bar{V}^{\mathrm{SIC}}_{\mathrm{xc},i\sigma}(t)=\langle\psi_{i\sigma}|\bar{V}^{\mathrm{SIC}}_{\mathrm{xc},\sigma}(\mathbf{r},t)|\psi_{i\sigma}\rangle$ and $\bar{v}_{i\sigma}(t)=\langle\psi_{i\sigma}|v_{i\sigma}(\mathbf{r},t)|\psi_{i\sigma}\rangle$. The TD OEP-SIC equations are solved for the individual time-dependent spin-orbital wave functions $\psi_{i\sigma}(\mathbf{r},t)$ in a self-consistent manner. Moreover, the single-particle time-dependent OEP-SIC is local (for every time step) and has the correct long-range $(-1/r)$ Coulombic potential behavior [16]. The advantages and recent applications of the TD OEP-SIC approach to various intense-field multiphoton processes are reviewed in [17].

The time evolution of the spin-orbital wave functions can be calculated accurately and efficiently by means of the TDGPS method [15–17]. The TDGPS consists of the following two essential steps: (a) the spatial coordinates are optimally discretized in a *nonuniform* spatial grid by means of the generalized pseudospectral technique [20] with the use of a very modest number of grid points. The mesh structure is characterized by denser grids near the origin and sparser grids for large distances. (b) A second-order split-operator technique in the *energy* representation, allowing the explicit elimination of undesirable fast-oscillating high-energy components, is used for the time propagation of the wave function [15],

$$\psi_{i\sigma}(\mathbf{r},t+\Delta t) \simeq e^{-i\hat{H}_0\Delta t/2}e^{-i\hat{V}(r,\theta,t+\Delta t/2)\Delta t}e^{-i\hat{H}_0\Delta t/2}\psi_{i\sigma}(\mathbf{r},t) + O(\Delta t^3). \tag{9}$$

The TDGPS technique has been shown to be both computationally considerably more efficient and accurate than the conventional time-dependent techniques using equal-spacing

grid discretization [15–17]. The norm of the field-free wave function is preserved to a high accuracy (~10 digits of accuracy) during the time propagation. Having determined the time-dependent spin-orbital wave functions $\psi_{i\sigma}(\mathbf{r},t)$, we then compute the time-dependent induced dipole moment as

$$d(t) = \int z\rho(\mathbf{r},t)d\mathbf{r} = \sum_{i\sigma} d_{i\sigma}(t), \tag{10}$$

where

$$d_{i\sigma}(t) = n_{i\sigma}\langle\psi_{i\sigma}(\mathbf{r},t)|z|\psi_{i\sigma}(\mathbf{r},t)\rangle \tag{11}$$

is the induced dipole moment of the ith spin orbital and $n_{i\sigma}$ is its electron occupation number. The power spectrum of the HHG is determined by taking the Fourier transform of the total time-dependent induced dipole moment $d(t)$ and scaling it to the one-pulse case

$$S(\omega) = \left|\frac{1}{N}\int_{t_i}^{t_f} d(t)e^{-i\omega t}dt\right|^2, \tag{12}$$

where N is the total number of pulsed used in the calculation and t_i and t_f are the initial and final times of the incident pulses, respectively.

The time-dependent (multiphoton) ionization probability of the ith spin orbital can be calculated according to $P_{i\sigma}(t) = 1 - N_{i\sigma}(t)$, where $N_{i\sigma}(t) = \langle\psi_{i\sigma}(\mathbf{r},t)|\psi_{i\sigma}(\mathbf{r},t)\rangle$ is the time-dependent survival probability of the ith spin orbital. Moreover, it is imperative to mention that all the electrons are treated explicitly and each contributes to the total effective potential and multiphoton processes.

Based on the TDDFT+OEP-SIC method, we shall now investigate the HHG process from He atoms in linearly polarized intense laser-pulse sequence. We first perform the calculations with the following laser parameters: 20-fs full width at half maximum (FWHM) Gaussian laser pulses of wavelength $\lambda = 800$ nm with peak intensities of $I = 5 \times 10^{13}$ W/cm^2 and $\Delta\phi = \pi/4$. The time delay τ between pulses is set to be 0.2 ps, allowing to expedite the numerical process and will not affect the coherence of the harmonics. Larger τ will also be used later on. Since the gas target embedded in the cavity focus will interact with about five to seven coherent excitation pulses before leaving the interaction region [11,12], a finite number of pulses will be used throughout the calculation.

We first compare the HHG spectrum for the one- and five-pulse excitation cases. When time-delayed coherence laser pulses are used ($N \geq 2$), quantum interference fringes clearly appear within each of the harmonic orders, as shown in Fig. 1(a), for the case of $N = 5$. The overall global pattern of the power spectra for the one-pulse excitation (denoted by red dots) and shown in Fig. 1(b) closely resembles to that formed by the five-pulse case (solid line). We found that a nested comb structure is formed within each harmonic order when more than one excitation pulse is utilized. The inset of Fig. 1(a), for instance, clearly displays the symmetric fringes formed around the 25th harmonic. In addition, $N-2$ interference substructures appear between adjacent comb modes. One can establish that the frequency comb of the fundamental mode formed by the pulse sequence is accurately transferred into each of the generated harmonics. Furthermore, we have thoroughly verified that the splitting between comb mode frequencies, also referred as the repetition frequency ω_r, is exactly given by $\omega_r = 2\pi/\tau$. These equally spaced discrete frequencies are essentially caused by constructive quantum interference emanating from the phase-locked induced dipole moments. In other words, the phase contributions θ_n, defined as $\tilde{d}_n(\omega) = |\tilde{d}_n(\omega)|e^{i\theta_n(\omega)}$ of separate induced nth-dipole pulses emanating from the pulse train, are identical at ω_r [14]. Here $\tilde{d}_n(\omega)$ is defined as the Fourier transform of the time-dependent induced dipole moment $d(t)$ integrated between the times $(n-1)\tau$ and $n\tau$.

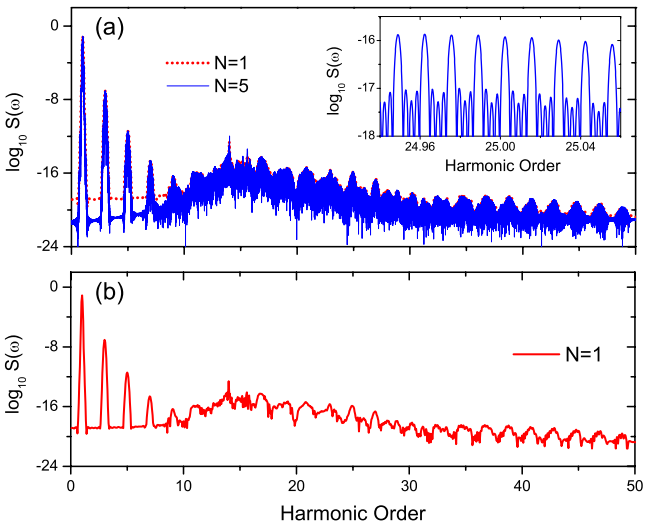

FIG. 1. (Color online) (a) The scaled HHG power spectrum $S(\omega)$ of He atom generated by one pulse (dotted line) and five successive 20-fs FWHM Gaussian pulses (solid line). A detailed view (inset, frequency resolution used is 10^{-4} a.u.) of the nested comb structure (for $N = 5$) is shown in the vicinity of the 25th harmonic. (b) Scaled HHG power spectrum $S(\omega)$ generated by $N = 1$ pulse. Laser intensity used is 5×10^{13} W/cm^2, wavelength is 800 nm, and $\tau = 0.2$ ps.

We note that at this relatively weak laser field, the intensity of the scaled power spectra $S(\omega)$ shows no considerable gain from the interaction of five pulses as obtained from the one-pulse case. To understand this feature we computed $P_{i\sigma}(t)$ for the He atom. Sequential ionization only occurs during each excitation pulse process as illustrated by the driving laser field in Fig. 2(a). A uniform staircase pattern visibly depicts the overall appearance of the ionization probability once the laser-pulse train is completed [see Fig. 2(b)]. The ionization probability from the $1s$ orbital increases rapidly during each of the pulse peak intensity. Beyond the pulse's peak intensity, the ionization probability reaches an ionization plateau region until the next pulse comes to interact with the atom. In relatively weak laser intensities where minimal ionization takes place and the neutral atom lingers as the dominant species, the laser field sees nearly the same population on the ground state. Hence, the ionization probability after each consecutive pulse remains nearly equal.

It is instructive to make a comparison of the results of the present all-electron TDDFT+OEP-SIC procedure to the conventionally used SAE model. As to be shown below, the

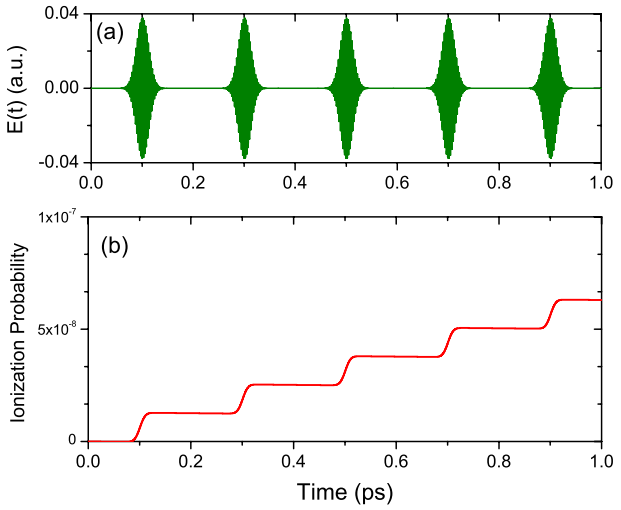

FIG. 2. (Color online) (a) Driving laser field composed of five successive 20-fs FWHM Gaussian pulses. (b) Ionization probability of He atom. Laser parameters used are the same as those in Fig. 1.

all-electron TDDFT formalism allows a detailed exploration of the effects of the dynamical electron correlation on ionization, HHG, and frequency comb coherence in a unified and self-consistent manner. In our SAE treatment, we perform the time-dependent OEP-SIC calculation with one of the 1*s* electron while the other electron is held frozen to the 1*s*, orbital similar to the procedure used in [16]. Figure 3(a) shows the comparison of the results of ionization probability of the He atom obtained from the all-electron TDDFT +OEP-SIC formalism (solid line) and the SAE model (dotted line) for the case of laser wavelength 800 nm, laser intensity 5×10^{13} W/cm^2, and τ=0.2 ps. It is seen that the SAE model predicts considerably larger ionization probabilities than those of the TDDFT calculations. We also found that the discrepancy increases with increasing laser intensity (not shown). The discrepancy can be understood by the following manner. In the actual time-dependent ionization process of the He atoms, the average electron binding energy of the atom should increase with time. This is due to the fact that when the atom is partially ionized (in terms of the ionization probability), the remaining electron (in terms of bound-electron probability) will be more tightly bounded due to the dynamical screening effect. For the He atom, the ionization potential of the neutral He atom is 0.904 a.u., while for the He^+ ion, the binding energy is 2.0 a.u. The all-electron TDDFT takes into account such a dynamical screening correlation or equivalently the dynamical electron correlation, while the SAE model does not consider that. Consequently, the SAE electron is always less bounded by the nucleus, leading to the overestimation of the ionization probability.

In Fig. 3(b), we present the comparison of the scaled HHG power spectrum density $S(\omega)$ obtained by the TDDFT+OEP-SIC method and the SAE model. For clarity, only the peak intensities of harmonics near the cutoff region are shown for comparison. We note that in general the SAE model tends to underestimate the harmonic power spectrum intensity for higher harmonics. Similar observation was predicted by our previous TDDFT study [16] and the recent fully *ab initio* two-electron six-dimensional (6D) calculations [21]. Figure 3(c) displays a detailed view of the nested comb structure in the vicinity of the 25th harmonic order for both TDDFT and SAE calculations. Despite the quantitative discrepancy, the SAE model is still capable of providing the frequency comb spectrum and coherence at least in a qualitative fashion. The deviation of the SAE results from the TDDFT data can be again attributed to the fact that the SAE model does not take into account the dynamical electron correlation.

We next investigate the effects of varying the pulse separation τ on the coherent properties of the frequency comb. Note that HHG processes occur over the duration of each individual pulse cycle only which is a much smaller time scale than the separation τ between successive pulses generated by a mode-locked femtosecond laser with a repetition

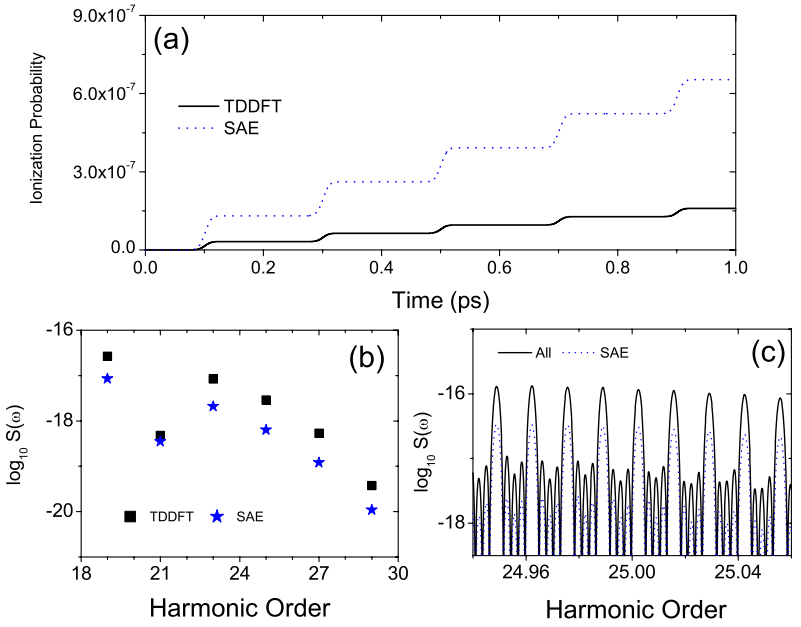

FIG. 3. (Color online) (a) The ionization probability of the He atom obtained from the TDDFT+OEP-SIC (solid line) and SAE (dotted line) calculations, respectively. It is seen that the SAE model predicts considerably larger ionization probabilities than those of the two-electron TDDFT calculations. (b) The scaled HHG power spectrum $S(\omega)$ of the He atom obtained from the TDDFT+OEP-SIC (black squares) and SAE (blue stars) calculations. For clarity, only the harmonic peak amplitudes are shown. (c) A detailed view of the nested comb structure in the vicinity of 25th harmonic order. Laser parameters used are the same as those in Fig. 1.

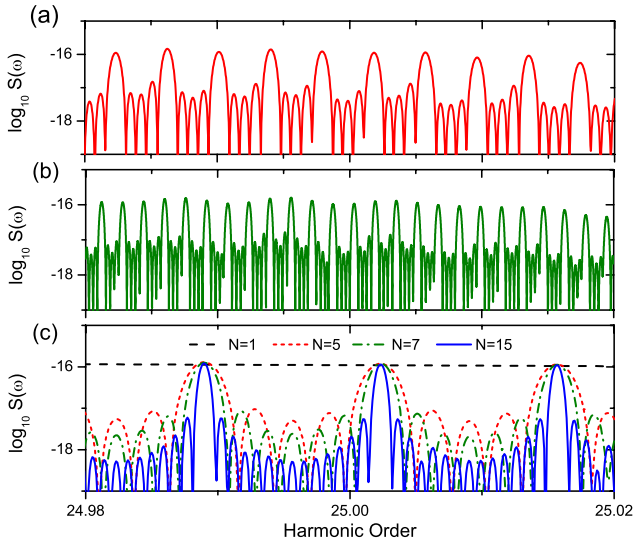

FIG. 4. (Color online) Detailed view of the nested comb structure in the vicinity of the 25th harmonic generated by a laser field of five successive 20-fs FWHM Gaussian pulses ($N=5$) for $\tau=$ (a) 10 ps and (b) 1 ns. (c) The HHG power spectra for $\tau=0.2$ ps in the vicinity of the 25th harmonic for $N=1$ (dash), $N=5$ (smaller dash), $N=7$ (dash dot) and $N=15$ (solid) pulse(s), respectively. The scaled HHG spectrum intensity $S(\omega)$ is invariant to N and the fringe resolution is enhanced as N increases. Laser intensity used is 5×10^{13} W/cm^2 and wavelength is 800 nm.

frequency of 100 Mhz (10 ns). Hence, the emitted HHG radiation should not be appreciably affected by the delay τ between pulses. Figures 4(a) and 4(b) show the harmonic spectra nearby the 25th harmonic for $N=5$ and $\tau=10$ ps and 1 ns, respectively. Other laser parameters are similar to those in Fig. 1. Since the repetition frequency ω_r is inversely proportional to τ, the comb mode separation decreases as τ is increased. In addition, the spectrum intensity $S(\omega)$ is nearly invariant to τ. Despite much extended time separations between pulses, we note that the coherent properties of the frequency comb fully prevail. Similar behavior was recently reported for the case of atomic H, where even for τ extending as long as 10 ns, the temporal coherence was still fully preserved [14].

The effects on the frequency comb structure and coherence as the pulse number N varies are then explored. Figure 4(c) shows the frequency comb structure (nearby the 25th harmonic) for $\tau=0.2$ ps for the case of $N=1$ (dash), 5 (smaller dash), 7 (dashed dot), and 15 (solid) pulse(s), respectively. Laser parameters other than N and τ are the same as those in Fig. 1. After varying the number of excitation pulses from $N=1$ to $N=15$, the contours of the power spectrum and the symmetry in the fringe shape remain unchanged. The comb's repetition frequency is fully preserved. Due to intrinsic interference effects, sets of $N-2$ additional peaks are present between adjacent comb fringes. In addition, the harmonic intensity $S(\omega)$ appears to be independent of N, but, as we will explore subsequently, it is not the case when stronger laser intensities are utilized. On the other hand, the spectral resolutions of the comb modes, being inversely proportional to N, are notably enhanced with increasing N. In the limit of implementing an infinite number of pulses, very sharp comb lines would be produced. Beyond these features, our results show that the coherence properties are essentially retained as N varies.

Next, we study the carrier-envelope phase coherence in the emitted HHG radiation by investigating in more detail the comb spectral spacing of the qth harmonic order. Since the driving pulse train is a frequency comb with frequencies Eq. (1), the generated photons, according to energy conservation, are sums of integer (odd) number of photons emanating from the driving field. The comb structure of the fundamental mode is then transferred to each of the qth harmonics in the xuv HHG spectrum. In this manner, the HHG spectrum now contains q frequency comb structures centered on each harmonic and the output of the qth harmonic-order results in a spectrum with frequencies given by Eq. (13) [12],

$$\omega'_m = m\omega_r + q\omega_0, \tag{13}$$

where the xuv comb frequencies are now $\omega'_m=q\omega_{m'}$ and the comb index integer m is given by qm'. To determine the phase coherence of HHG, we shall define the spectral shift as $\delta=q\omega_0=q\Delta\phi\omega_r/2\pi$ and monitor δ as a function of q and $\Delta\phi$, respectively.

We calculate the HHG power spectra and ionization probabilities for each of the following cases: $\Delta\phi=0,\pi/16,\pi/8$ for $N=5$, $\tau=0.2$ ps, and a laser intensity of 5×10^{13} W/cm^2. Figures 5(a)–5(c) illustrate the comb structure around $q=5$, 17, and 25 harmonic orders, respectively, for $\Delta\phi=\pi/16$ (thick red line). We compare them to $S(\omega)$ when the pulse-to-pulse phase shift is doubled to $\Delta\phi=\pi/8$ (thick blue line) and shown in Figs. 5(d)–5(f), respectively. The corresponding results for $\Delta\phi=0$ (thin lines) serve as the reference frequencies. First, $P_{i\sigma}(t)$ (not shown) at the end of the pulse train is completely independent of $\Delta\phi$ used. As a result, we observe that the $S(\omega)$ intensity for various cases of $\Delta\phi$ remains nearly constant and ω_r is fully preserved. Afterward, Figs. 5(a)–5(c) illustrate how the spectral shift δ or the spacing between the reference comb line $\Delta\phi=0$ and the concerned comb line ($\Delta\phi=\pi/16$) increases (shown between arrows) according to the harmonic order q. The linear dependence of δ on q can be more clearly distinguished by comparing, for example, the spacing between $q=5$ and $q=25$ for $\Delta\phi=\pi/16$ [Figs. 5(a) and 5(c)] and observing that the spectral shift δ also increases by a factor of 5. Similar results are obtained for the case of $\Delta\phi=\pi/8$ [Figs. 5(d) and 5(f)]. To check the δ dependence on $\Delta\phi$, it is enough to show that for a given harmonic, for instance, $q=5$ [Figs. 5(a) and 5(d)], the spectral spacing doubles as $\Delta\phi$ doubles. Similar findings can be observed for $q=17$ [Figs. 5(b) and 5(e)] and $q=25$ [Figs. 5(c) and 5(f)], respectively. Consequently, the phase shift δ under weak to medium-laser fields is linearly dependent on q and $\Delta\phi$, indicating the phase coherence is fully preserved and Eq. (13) is valid. To determine the degree of coherence among the emitted HHG during each excitation pulse, we perform a time-frequency analysis of the frequency comb spectrum below.

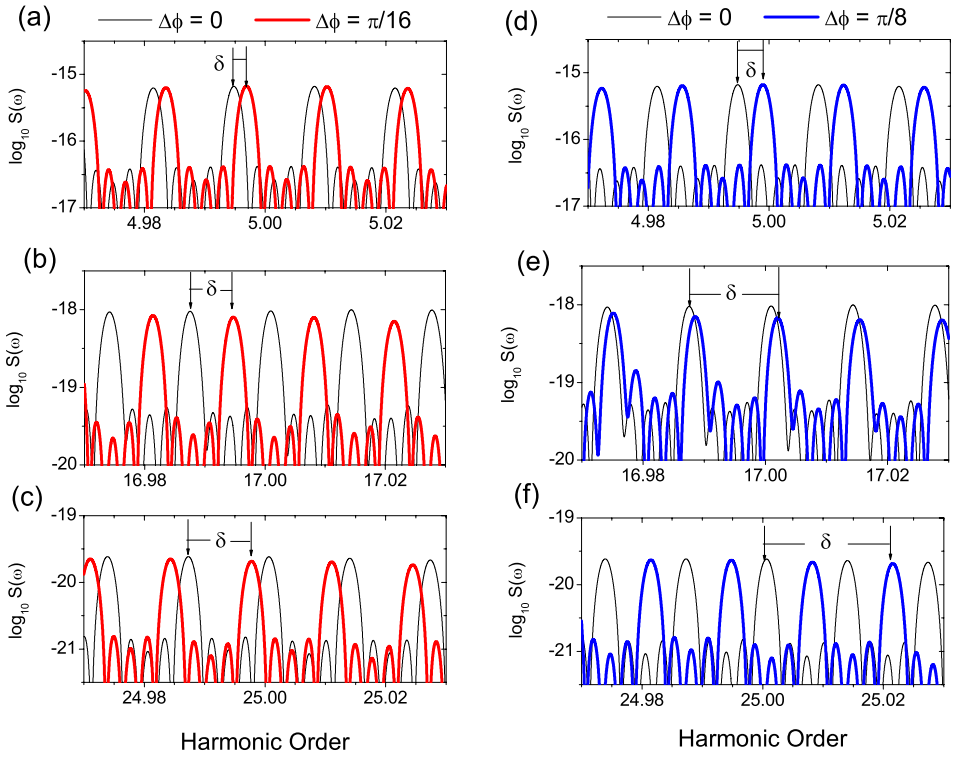

FIG. 5. (Color online) Scaled harmonic power spectra $S(\omega)$ generated by a train of five ($N=5$) 20-fs FWHM Gaussian pulses near the (a) fifth, (b) 17th, and (c) 25th harmonic for $\Delta\phi=\pi/16$ and [(d)–(f)] for $\Delta\phi=\pi/8$, respectively. The carrier-envelope phase coherence is fully maintained in the emitted radiation. Laser intensity is 5×10^{13} W/cm^2, wavelength is 800 nm, $\tau=0.2$ ps, and the frequency resolution is 10^{-5} a.u.

III. WAVELET TIME-FREQUENCY ANALYSIS OF THE FREQUENCY COMB SPECTRUM

To explore the details of the quantum mechanisms involved in the formation of harmonic interference, we investigate the HHG time-frequency profiles $|d_{\omega_q}(t)|$, obtained from the wavelet time-frequency analysis of the induced dipoles $d(t)$ [22–25],

$$d_{\omega_q}(t) = \sqrt{\frac{\omega_q}{\sigma}} \int d(t) e^{i\omega_q(t-t_0)} e^{-[\omega_q(t-t_0)]^2/2\sigma^2} dt, \quad (14)$$

where $\omega_q=q\omega_c$, ω_c is the fundamental laser angular frequency, and q is the harmonic order. In the discussion below, we choose $\sigma=10$ to perform the wavelet transform. Figures 6(a)–6(e) show successive time profiles [Fig. 6(a) for the first pulse, Fig. 6(b) for the second pulse, etc.] for the cases of $N=5$, $q=45$, and $\Delta\phi=\pi/32$. For the laser intensity of 5×10^{13} W/cm^2, where minute ionization takes place [see Fig. 2(b)], the magnitude of the time-dependent profile $|d_{\omega_q}(t)|$ during each pulse remains nearly unchanged. We note that in each of the time profiles corresponding to each of the incident pulses, two dominant emissions occur within each optical cycle, indicating that only one returning (short) trajectory has the largest contribution. This characteristic is especially indicative of harmonics in the cutoff region. Similar characteristics are observed in harmonics ranging from 31st up to 49th harmonic order (not shown). Emission times corresponding to these harmonics nearly coincide during each of the five pulses, suggesting a high degree of spectral synchronization emanating from each pulse. On the other hand, time profiles for harmonics in the plateau region exhibit more than two emissions per laser optical cycle as a result of the contributions from the short and long trajectories [26]. Results for the harmonic in the plateau region, $q=21$, are presented in Figs. 7(a)–7(c) corresponding to the first, third, and fifth pulses, respectively. Indeed, the time profiles display more than two emissions occurring within each optical cycle indicating contributions from both trajectories. Furthermore, to determine the coherence character of the emitted HHG radiation among successive pulses, we compute the dynamical phase $\varphi[\omega_q(t_e)]$ from the wavelet analysis of the induced dipoles. Note that the dipole time profile at harmonic frequency ω_q, the dynamical phase, and the recollision time (t_e) are related to each other by the following expression [24]:

$$d_{\omega_q}(t_e) = |d_{\omega_q}(t_e)| e^{-i(\omega_q t_e + \varphi[\omega_q(t_e)])}. \quad (15)$$

Here the peak emission times t_e, corresponding to the maxima of the dipole time profiles, can be interpreted semiclassically as the electron-ion recollision times [24]. Results of the dynamical phase $\varphi[\omega_q(t)]$ calculations are displayed in Figs. 6(a)–6(e) (denoted by solid dots). At this relatively weak laser intensity, the comb structure of the fundamental mode is fully transferred to each of the harmonic orders. Moreover, the dynamical phase's behavior of a given harmonic during the first pulse should have a high degree of resemblance to that obtained from the other consecutive pulses if the ground-state population is nearly the same (or when the ionization probability is very small) in each pulse. Indeed, we note that the overall magnitude of the dynamical phases among different pulses is nearly uniform and encompassing only up to 2 rad during the sequence of pulses. In addition, the dynamical phases increase slightly and homogeneously with each successive pulse. We monitor $\varphi[\omega_q(t_e)](q=45)$ during six consecutive peak emissions [denoted A–F in Fig. 6(a)] occurring in each of the atom-laser

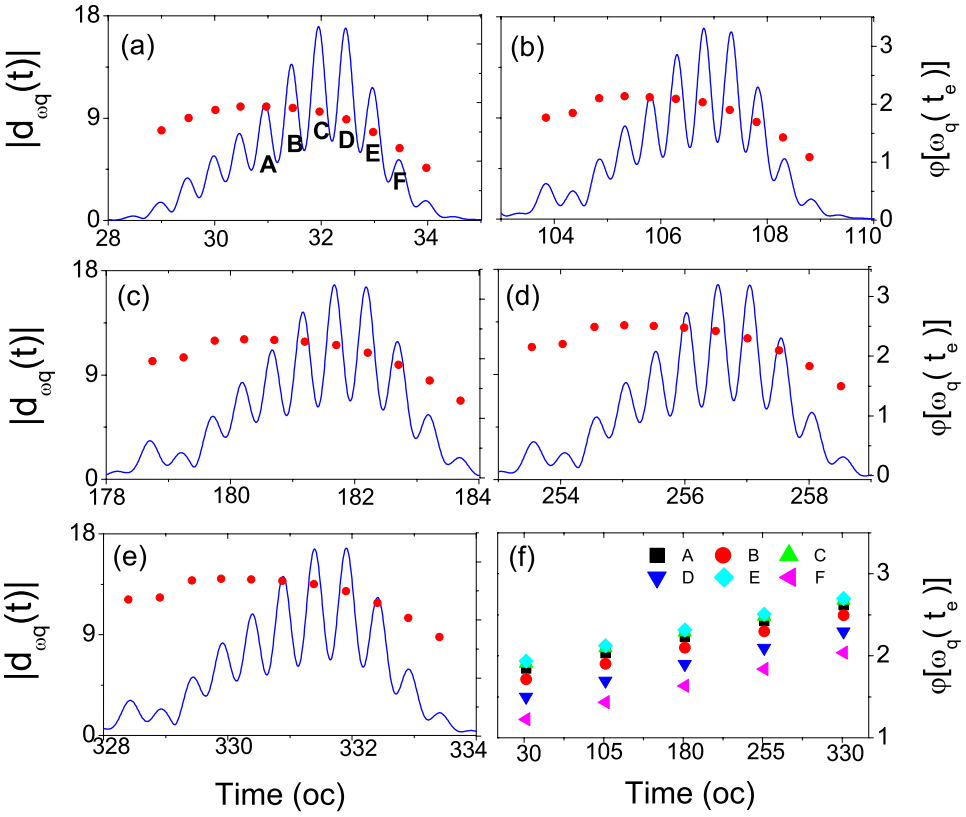

FIG. 6. (Color online) [(a)–(e)] Dipole time profiles (in the unit of 10^{-11} a.u.) of the $q=45$ harmonic order corresponding to each successive pulse produced by a train of five ($N=5$) 20-fs FWHM Gaussian pulses and their corresponding dynamical phases $\varphi[\omega_q(t_e)]$ (denoted by solid dots, in radians) calculated at the "peak" emission times. (f) The dynamical phase during each emission time (denoted by A–F) increases homogeneously with each successive pulse. The laser intensity is 5×10^{13} W/cm^2, wavelength is 800 nm, $\Delta\phi=\pi/32$, $\tau=0.2$ ps, and the time resolution is 0.01 a.u. The time is measured in units of the field period $T=2\pi/\omega_c$.

interactions. Our calculations demonstrate that $\Delta\varphi$ between two consecutive pulses for a given emission peak is indeed nearly constant ($\Delta\varphi=0.2\pm0.01$ rad). Figure 6(f) shows the linear dependence of $\varphi[\omega_q(t_e)]$ with the excitation pulses. The observed coherence of the frequency comb may be associated to the fact that there is a constant phase difference among subsequent pulses, as depicted in Fig. 6(f). In addition, the span of which $\Delta\varphi$ varies directly depends on the pulse-to-pulse phase shift $\Delta\phi$ and it is independent whether the harmonic belongs to the plateau or the cutoff region. In the case of the plateau harmonic, we monitor the emission peaks labeled A–F, as seen in Fig. 7(a), throughout the train of pulses and obtain a similar linear dependence as noted above. However, for the plateau harmonic, we observe that the extent at which $\Delta\varphi$ varies is at least 4 times greater than that of the cutoff harmonic. Despite the significant range of $\Delta\varphi$, the robustness of the comb fringes in each harmonic is still fully maintained.

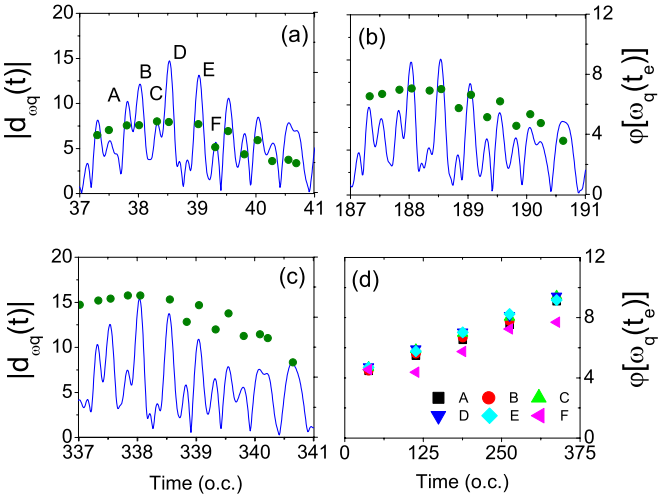

FIG. 7. (Color online) Dipole time profiles (in the unit of $\times10^{-9}$ a.u.) of the 21th harmonic order corresponding to the (a) first, (b) third, and (c) fifth pulses produced by a train of ($N=5$) Gaussian pulses and their corresponding dynamical phases $\varphi[\omega_q(t_e)]$ (denoted by full circles, in radians) calculated at the "peak" emission times. (d) The dynamical phase during each emission time (denoted by A–F) increases homogeneously with each successive pulse. Laser parameters used are the same as those in Fig. 6

IV. IONIZATION DEPHASING EFFECTS IN STRONG FIELDS

Here, we will extend our investigation by studying the effects on the frequency comb structure and coherence under superstrong intensity laser fields. We explore the possible ionization dephasing effects as strong laser fields largely ionize the atom. First of all, under the influence of strong laser fields, we note that the increase of the ionization probability of He atoms is no longer uniform in amplitude during each of the consecutive pulses. For instance, Figs. 8(a)–8(c) illustrate the extent of ionization taking place for the laser intensity of 9×10^{14} W/cm^2 after one ($N=1$), five ($N=5$), and seven ($N=7$) pulses, respectively. The He atom undergoes a more substantial ionization at the end of the first pulse than the succeeding pulses. The difference in ionization probability among pulses is more apparent in the case of stronger

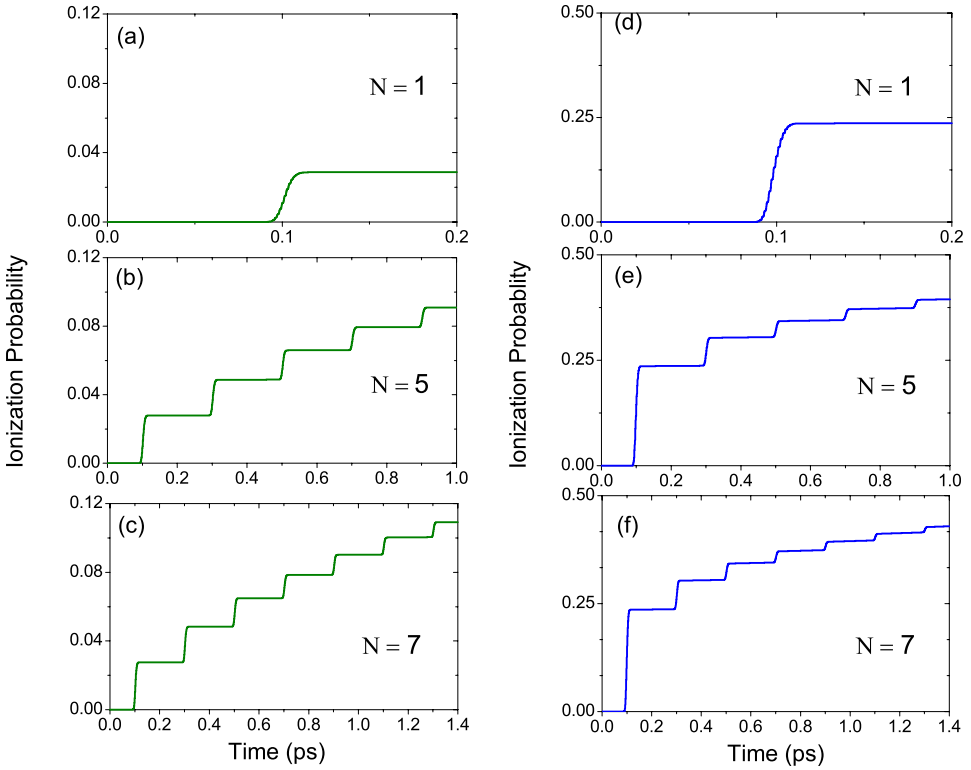

FIG. 8. (Color online) Time-dependent ionization probabilities for He atom for $N=1$, $N=5$, and $N=7$ (20-fs FWHM) Gaussian pulses under laser field intensities of [(a)–(c)] 9×10^{14} W/cm^2 and [(d)–(f)] 2×10^{15} W/cm^2. Uneven ionization between pulses takes place under strong laser fields. The wavelength used is 800 nm and $\tau=0.20$ ps.

laser fields such as 2×10^{15} W/cm^2 shown in Figs. 8(d)–8(f). Indeed, at the end of the first pulse, more than half of the total ionization probability takes place, as seen in Figs. 8(e) and 8(f). Conversely, the last pulses will contribute the least to the total ionization as shown in Figs. 8(b) and 8(c) for 9×10^{14} W/cm^2 and in Figs. 8(e) and 8(f) for 2×10^{15} W/cm^2, respectively. As the laser intensity increases, the ground-state population becomes partially depleted in each of the instances the atom encounters a pulse. In this manner, after the first pulse excitation, the ground-state population will be less than 100%. When the next pulse interacts with the atom, the amount ionized will not be the same to that of the first pulse excitation since the initial-state population for the second pulse is no longer the same as that

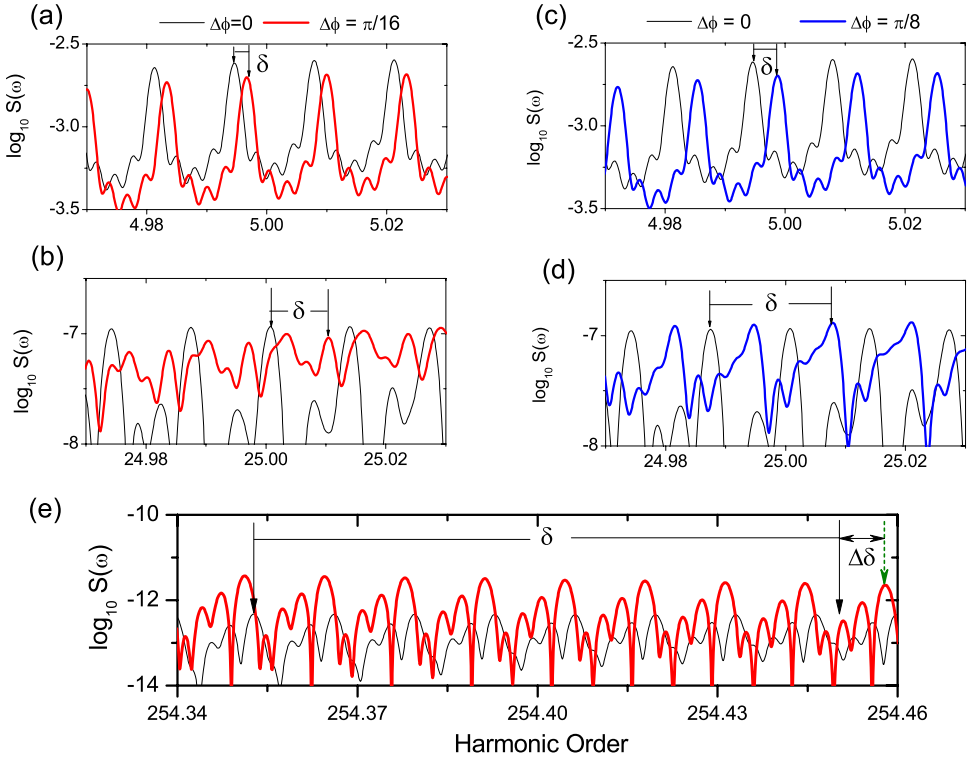

FIG. 9. (Color online) Scaled harmonic power spectra generated by a train of five ($N=5$) 20-fs FWHM Gaussian pulses near the (a) 5th and (b) 25th harmonics for $\Delta\phi=\pi/16$ and [(c) and (d)] for $\Delta\phi=\pi/8$, respectively. (e) The blueshifted 255th harmonic. The carrier-envelope phase coherence is only partially maintained in the emitted radiation. Laser intensity is 2×10^{15} W/cm^2, wavelength is 800 nm, $\tau=0.2$ ps, and the frequency resolution is 10^{-5} a.u.

of the first pulse. In addition, as the atom is partially ionized (in terms of the ionization probability), the remaining electron will be more tightly bounded by the nucleus due to the dynamical screening effect. Hence, the average electron binding energy of the remaining electron density increases with time, making it more difficult for the electron to detach. Consequently, the step amplitudes in the ionization probability will not be identical. Also, He^+ may become the dominant species when large ionization takes place. He^+ is much more difficult to ionize due to its substantially larger ionization potential than that of the neutral atom and the ionization probability should decrease from pulse to pulse [16].

Next, we study the carrier-envelope phase coherence in the emitted HHG radiation by investigating the comb spectral spacing of the qth harmonic order in strong laser fields. We calculate $S(\omega)$ for each of the following cases: $\Delta\phi = 0, \pi/16, \pi/8$ for $N=5$, $\tau=0.2$ ps, and a laser field intensity of 2×10^{15} W/cm^2. Figures 9(a) and 9(b) show, respectively, the comb structure around the $q=5$ and 25 harmonic orders for $\Delta\phi=\pi/16$ (thick red line). For the case of $\Delta\phi = \pi/8$ (thick blue line), the results are displayed in Figs. 9(c) and 9(d), respectively. We observe, for example, in the case of $\Delta\phi=\pi/16$ [Figs. 9(a) and 9(b)] that the spectral shift δ (shown between arrows) between harmonics $q=5$ and $q=25$ also increases proportionally to q. Likewise, δ increases by a factor of 2 when $\Delta\phi$ is doubled as illustrated for the harmonic $q=5$ [Figs. 9(a) and 9(c)]. Thus the linear dependences of δ on q and $\Delta\phi$ remain valid for lower harmonics. However, cutoff harmonics which suffer the largest blueshift due to the nonadiabatic effect caused by the rapid increase of the laser electric field [27] do not follow well the linearity proposed in Eq. (13). For example, Fig. 9(e) shows the deviation $\Delta\delta$ between the expected δ obtained from Eq. (13) (solid arrow) and the calculated position (dashed arrow) of the interference comb. Since the blueshift increases with harmonic order q, it is much smaller for lower harmonics. As a result, Eq. (13) can be considered valid only for these lower harmonics. On the other hand, as the blueshift becomes more important as in the case for the cutoff harmonics, the linearities of δ on q and $\Delta\phi$ are no longer valid. Hence, this deviation $\Delta\delta$ can be attributed in part to the fact that Eq. (13) does not take into account the blueshift that high-frequency harmonics undergo through.

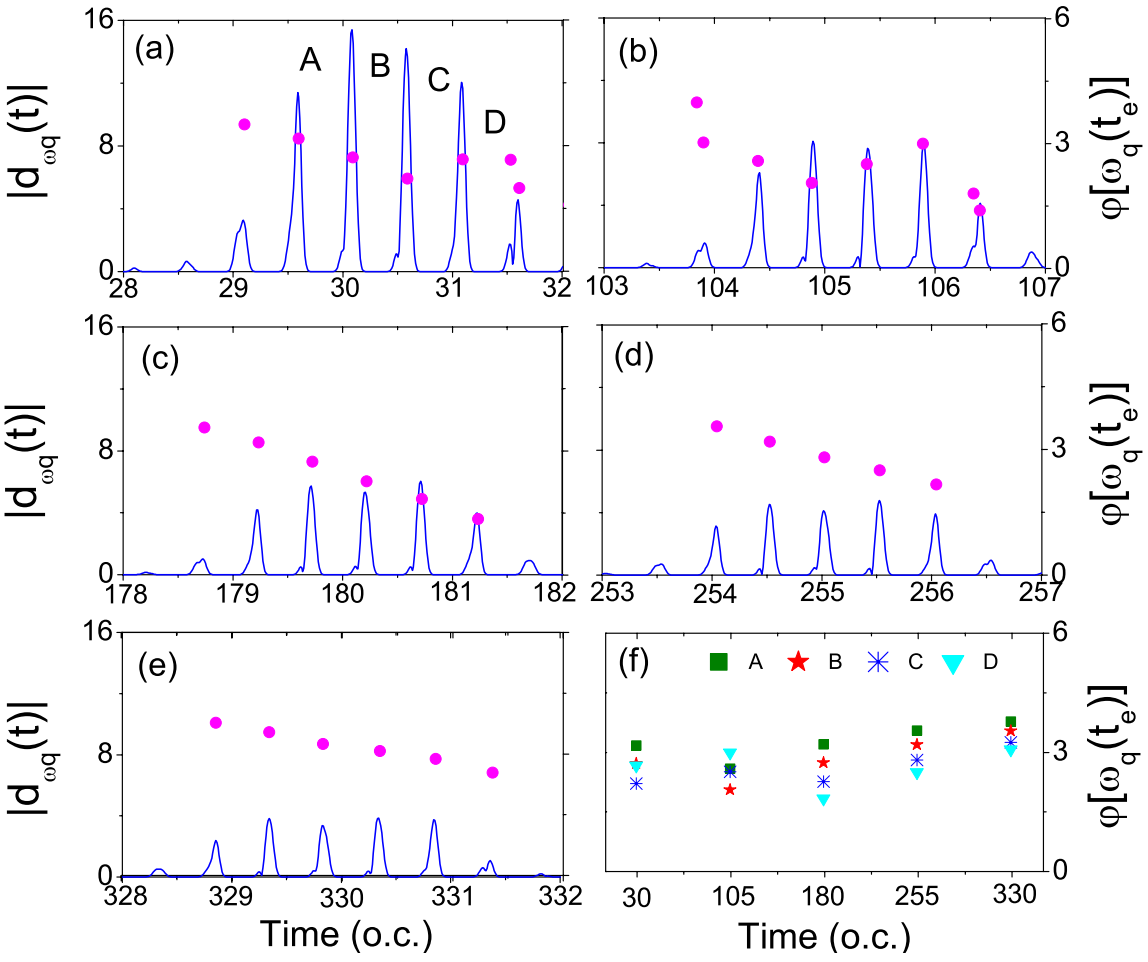

FIG. 10. (Color online) [(a)–(e)] Dipole time profiles (in the unit of 10^{-6} a.u.) of the 245th harmonic corresponding to each successive pulse produced by a train of (N=5)20 fs FWHM Gaussian pulses and their corresponding dynamical phases $\varphi[\omega_q(t_e)]$ (denoted by solid dots, in radians) calculated at "peak" emission times. (f) The dynamical phase does not increase homogeneously during each emission time (denoted by A–D) with each successive pulse and the comb coherence is lost. The laser intensity is 2×10^{15} W/cm^2, wavelength 800 nm, $\Delta\phi=\pi/8$, $\tau=0.2$ ps, and the time resolution is 0.01 a.u.

Finally, we present the time-frequency wavelet analysis for the case of $N=5$ and laser intensity of 2×10^{15} W/cm^2, as shown in Fig. 10. We observe that the magnitude of the time-dependent dipole profile $|d_{\omega_q}(t)|$ for the 245th harmonic varies from pulse to pulse, as illustrated in Fig. 10(a) for the first pulse, Fig. 10(b) for the second pulse, etc. The first two pulses see the most significant decrease in magnitude. This characteristic is closely related to the distinct extent of ionization taking place during the first and the second pulses as shown in Figs. 6(e) and 6(f), respectively. Since the extent of ionization is nearly the same among the last three pulses [see Fig. 6(e)], their corresponding dipole time profiles are also similar in scale among each other. Results of the dynamical phase $\varphi[\omega_q(t)]$ calculations for each of the five pulses are displayed accordingly in Figs. 10(a)–10(e) (denoted by filled circles). Since the ionization contributions resulting from the last three pulses are very similar among each other, $\varphi[\omega_q(t_e)]$ for these pulses shows a more homogeneous pattern. We monitor $\varphi[\omega_q(t)]$ during four consecutive peak emissions [denoted A–D in Fig. 10(a)] and show the results in Fig. 10(f). We note that spectral phase locking among pulses is rather poor. Indeed, the difference in dynamical phase $\Delta\varphi$ between pulses for any given emission event is not constant anymore, indicating the loss of temporal coherence. The comb interference structures in some instances are not fully symmetrical and now show secondary peaks between the actual interference fringes as observed in Figs. 9(b), 9(d), and 9(e). The $N-2$ substructures between fringes are completely washed out.

V. CONCLUSION

We have presented an *ab initio* nonperturbative investigation of the frequency comb structure and coherence within each order of the HHG of rare-gas atoms by means of the TDDFT with OEP and SIC. The TDDFT+OEP-SIC equations are solved accurately and efficiently by means of the time-dependent generalized pseudospectral technique. In addition, we also perform the SAE model calculation for the comparison. We found that it is significant to include the dynamical electron correlation, which is included in the TDDFT+OEP-SIC formalism but not the SAE model, for the quantitative exploration of the strong-field ionization, HHG, and frequency comb structure and coherence. For the frequency comb study, it is seen that a nested comb structure appears within each of the harmonics, ranging from the first harmonic all the way to the cutoff harmonics in weak and medium strong laser fields. The frequencies of the comb spectrum nested in each the harmonics are equally spaced by the repetition frequency which is inversely proportional to the time separation of the pulses. As the number of pulses interacting with He atom increases, the more ionization the atom will undergo and the greater the resolution of the comb fringes is obtained. The time-frequency characteristics of the HHG coherence structure are analyzed in details by means of the wavelet transform of the time-dependent induced dipole moment. The frequency comb interference modulation can be attributed to the phase locking of harmonics among successive pulses. However, under very strong laser fields from which atomic ionization is rather substantial, the frequency comb coherence is not longer preserved in the single-atom response. In addition, significant ionization will have also strong effects on the phase matching during time propagation as well. Thus to ensure the full frequency comb structure and coherence in high harmonics, it is advantageous to use only weak or medium strong laser field strengths in the experimental studies.

ACKNOWLEDGMENTS

This work is partially supported by the Chemical Sciences, Geosciences, and Biosciences Division of the Office of Basic Energy Sciences, Office of Sciences, U.S. Department of Energy and by the U.S. National Science Foundation. We also would like to acknowledge the partial support of National Research Council of Taiwan (Contract No. 97-2112-M-002-003-MY3) and National Taiwan University (Contract No. 97R0066).

[1] M. Fischer, N. Kolachevsky, M. Zimmermann, R. Holzwarth, Th. Udem, T. W. Hänsch, M. Abgrall, J. Grünert, I. Maksimovic, S. Bize, H. Marion, F. Pereira Dos Santos, P. Lemonde, G. Santarelli, P. Laurent, A. Clairon, C. Salomon, M. Haas, U. D. Jentschura, and C. H. Keitel, Phys. Rev. Lett. **92**, 230802 (2004).

[2] H. S. Margolis, G. P. Barwood, G. Huang, H. A. Klein, S. N. Lea, K. Szymaniec, and P. Gill, Science **306**, 1355 (2004).

[3] R. Holzwarth, Th. Udem, T. W. Hänsch, J. C. Knight, W. J. Wadsworth, and P. St. J. Russell, Phys. Rev. Lett. **85**, 2264 (2000).

[4] J. Stenger, T. Binnewies, G. Wilpers, F. Riehle, H. R. Telle, J. K. Ranka, R. S. Windeler, and A. J. Stentz, Phys. Rev. A **63**, 021802(R) (2001).

[5] M. Takamoto, F.-L. Hong, R. Higashi, and H. Katori, Nature (London) **435**, 321 (2005).

[6] S. A. Diddams, Th. Udem, J. C. Bergquist, E. A. Curtis, R. E. Drullinger, L. Hollberg, W. M. Itano, W. D. Lee, C. W. Oates, K. R. Vogel, and D. J. Wineland, Science **293**, 825 (2001).

[7] M. Hentschel, R. Kienberger, Ch. Spielmann, G. A. Reider, N. Milosevic, T. Brabec, P. Corkum, U. Heinzmann, M. Drescher, and F. Krausz, Nature (London) **414**, 509 (2001).

[8] M. Drescher, M. Hentschel, R. Kienberger, G. Tempea, C. Spielmann, G. A. Reider, P. B. Corkum, and F. Krausz, Science **291**, 1923 (2001).

[9] S. T. Cundiff and J. Ye, Rev. Mod. Phys. **75**, 325 (2003).

[10] K. S. E. Eikema, J. Walz, and T. W. Hänsch, Phys. Rev. Lett. **86**, 5679 (2001).

[11] R. J. Jones, K. D. Moll, M. J. Thorpe, and J. Ye, Phys. Rev. Lett. **94**, 193201 (2005).

[12] C. Gohle, T. Udem, M. Herrmann, J. Rauschenberger, R. Holzwarth, H. A. Schuessler, F. Krausz, and T. W. Hänsch,

Nature (London) **436**, 234 (2005).
[13] F. Lindner, W. Stremme, M. G. Schätzel, F. Grasbon, G. G. Paulus, H. Walther, R. Hartmann, and L. Strüder, Phys. Rev. A **68**, 013814 (2003).
[14] J. J. Carrera, S. K. Son, and Shih-I Chu, Phys. Rev. A **77**, 031401(R) (2008).
[15] X. M. Tong and S. I. Chu, Chem. Phys. **217**, 119 (1997).
[16] X. M. Tong and Shih-I Chu, Phys. Rev. A **57**, 452 (1998).
[17] S. I. Chu, J. Chem. Phys. **123**, 062207 (2005).
[18] C. A. Ullrich, U. J. Gossmann, and E. K. U. Gross, Phys. Rev. Lett. **74**, 872 (1995).
[19] J. Chen, J. B. Krieger, Y. Li, and G. J. Iafrate, Phys. Rev. A **54**, 3939 (1996).
[20] G. H. Yao and S. I. Chu, Chem. Phys. Lett. **204**, 381 (1993).
[21] X. Guan, X. M. Tong, and Shih-I Chu, Phys. Rev. A **73**, 023403 (2006).
[22] P. Antoine, B. Piraux, and A. Maquet, Phys. Rev. A **51**, R1750 (1995).
[23] M. B. Gaarde, Ph. Antoine, A. L'Huillier, K. J. Schafer, and K. C. Kulander, Phys. Rev. A **57**, 4553 (1998).
[24] X. M. Tong and Shih-I Chu, Phys. Rev. A **61**, 021802(R) (2000).
[25] X. Chu and Shih-I Chu, Phys. Rev. A **64**, 021403(R) (2001); **63**, 023411 (2001).
[26] Ph. Antoine, A. L'Huillier, and M. Lewenstein, Phys. Rev. Lett. **77**, 1234 (1996).
[27] H. J. Shin, D. G. Lee, Y. H. Cha, J.-H. Kim, K. H. Hong, and C. H. Nam, Phys. Rev. A **63**, 053407 (2001).